Computers and Mathematics with Applications 100 (2021) 182–195

Contents lists available at ScienceDirect

Computers and Mathematics with Applications

www.elsevier.com/locate/camwa

A partitioned solver for compressible/incompressible fluid flow and light structure

Deepak Garg *, Paolo Papale, Antonella Longo

Istituto Nazionale di Geofisica e Vulcanologia, Sezione di Pisa, Via Cesare Battisti, 53, 56125 Pisa, Italy

ARTICLE INFO

Dataset link:
https://codeocean.com/capsule/6716089/tree/v1

Keywords:
Fluid-structure interaction
Finite element method
Compressible-incompressible flow
SUPG stabilization
Dirichlet-Neumann partitioning
Lightweight structures

ABSTRACT

In this work, a partitioned fluid-structure interaction solver is presented. Fluid flow problem is solved with time-discontinuous deforming domain stabilized space-time finite element method. Flow is computed with pressure primitive variables which permit to use the same numerical technique for both compressible and incompressible regimes. Elastic deformation of the structure is modelled in the Lagrangian frame of reference with Saint-Venant Kirchhoff and Neo-Hookean material models - both are non-linear and valid for large deformations. Structure equations are discretized with Galerkin finite element method for space and with generalized-alpha method for the time. Mesh motion is modelled with the elastic deformation method. An implicit algorithm is presented to couple the different solvers. The details are provided on the implementation of the solvers in parallel software. The numerical code is verified and validated on several compressible and incompressible flow benchmarks widely used in the literature. The results demonstrate that the developed solver successfully detects the accurate interaction between fluid and structure.

1. Introduction

Fluid-structure interaction (FSI) problems often involve a light structure and a viscous fluid and are known for their complex multi-physics nature. FSI is one of the most challenging categories of the problems in computational mechanics. The problems encounter stability issues, especially when the fluid is highly viscous, and the structure is thin and light. Over the last few decades FSI problems have gained enormous attention due to their vast number of applications in the field of aeroelasticity [12,35], turbomachinery [30,75] and parachute dynamics [65,58,59]. FSI also plays a crucial role in the design and analysis of micro-air-vehicles [51,55] and heat exchangers [38,40]. FSI has been successfully employed to analyze the flow structure in hemodynamic problems [6,31].

In general, FSI problems are modelled in two ways: monolithic [65,59,67,32,7] and segregated [16,24,37,70,49]. In the monolithic approach fluid, structure and mesh motion equations are solved simultaneously, discretizing the coupled non-linear system in a unified way. This method takes into account fluid-structure mutual interactions directly and is known for its stability, robustness and handling of complex non-linear problems, particularly, where light structure and heavy fluid are involved. However, monolithic methods are less modular and require writing a fully-coupled FSI solver. Apart from that, monolithic solvers also suffer while solving large sparse fluid-structure-combined linear systems as it is difficult to design a suitable preconditioner for FSI problems. In segregated or partitioned approach, the fluid, structure and mesh motion equations are solved sequentially, in uncoupled fashion, and their coupling is done by appropriate boundary conditions acting at the fluid-structure interface. The coupling in the partitioned FSI solvers can further be classified as weak [45] or strong [49]. The partitioned approach has been successfully applied to various FSI problems [16,49,37]. Ease and flexibility to use the existing fluid, structure and mesh motion solvers make the partitioned approach a preferred choice.

Solving an FSI problem by a partitioned approach consists of three parts. The first one is to solve for fluid flow. In FSI problems, the computational domain for the flow deforms according to interface displacement, requiring, therefore, a flow solver appropriate for deforming meshes. We use Deforming-spatial-domain FEM (ST) to solve flow problems [62,64,59]. The method is based on the stabilized finite element formulation and is

The code (and data) in this article has been certified as Reproducible by Code Ocean: https://codeocean.com/. More information on the Reproducibility Badge Initiative is available at https://www.elsevier.com/physical-sciences-and-engineering/computer-science/journals.

* Corresponding author.
E-mail address: deepak.garg@ingv.it (D. Garg).

https://doi.org/10.1016/j.camwa.2021.09.005
Received 3 February 2021; Received in revised form 5 August 2021; Accepted 11 September 2021
Available online 27 September 2021

written over the space-time domain of a fluid mechanics problem [27,47,54]. The stabilization prevents numerical instabilities in the presence of advection dominated flows and allows the use of equal-order interpolation functions for solution variables. The numerical scheme has been effectively used to compute compressible/incompressible flows with fixed and moving domains [19,20]. In [42] the ST method was extended for multi-fluid problems and has been used to study geophysical flow problems [43,52,21]. In [71] the method was extended by defining weakly enforced essential boundary conditions and sliding interfaces for compressible flows and was used for gas-turbine and rotorcraft modelling. An isogeometric analysis of compressible flows with stabilised methods was presented in [72,9]. In the ST method, mesh velocity terms appear inherently in the ST formulation. Moreover, the geometric conservation law is automatically satisfied in the ST method. In the arbitrary-Lagrangian-Eulerian (ALE) method [57,7], conservation equations need to include mesh velocity terms explicitly. However, in [47], the authors show that ST and ALE methods are equivalent.

The second part of the partitioned approach method for FSI problems is to solve for the structure. In general, elastic deformation is modelled by the Hook's law [33], which is linear and applicable only for small displacements. For excessive bending and rotation, often appearing in FSI problems, non-linear constitutive models such as Saint-Venant Kirchhoff and Neo-Hookean are more suitable [46,56].

The third part is to compute mesh motion for internal fluid mesh nodes subject to moving solid domain. For mesh deformation, several methods have been proposed in the literature, such as Laplacian [41], biharmonic [29], spring [4], transfinite interpolation [15] and elastic deformation [44,64].

Over the years, many sophisticated methods have been developed for both compressible [25,66,71,72] and incompressible [64,73] flows. The common approach in modelling FSI problems is to develop software specific for either compressible or incompressible flow. In fact, solving those two regimes within a single numerical scheme is not straightforward [26,27,76,13,74], and it becomes even more complex when FSI is involved. However, many problems from the real world require a capability to handle the two regimes simultaneously. A relevant example comes from volcanic eruptions [61]: the magma moving at depths of order some km below the Earth surface, where shallow magmatic reservoirs are located, is close to incompressible [43,52,21]. However, while ascending and decompressing the initially dissolved volatiles separate into an expanding and accelerating gas phase, and the gas-pyroclast mixture leaving the volcanic vent and intruding the atmosphere is highly compressible and normally supersonic [1]. Solving for magma motion and associated rock dynamics allows us to relate measured rock displacements to deep magma movements and anticipate the occurrence of potentially destructive eruptions. However, it strictly requires an FSI solver which can continuously treat flows with Mach numbers from vanishingly small to largely above 1.

In spite of considerable progress during recent decades in solving FSI problems [59,37,24,60,50], there is still substantial need for a robust unified method for situations like the one above, where the fluid interacting with the solid can be from incompressible to supersonic at different locations in space and time. Here we contribute with a novel partitioned FSI method that couples a flow solver applying from incompressible to compressible flows to a solid mechanics solver, and that extends our previous studies on compressible/incompressible flows in fixed domains with or without free surface [19,20]. To use a unified solver for both compressible and incompressible flows, we employ pressure primitive variables instead of conservation variables as unknowns [27]. The incompressible limit of compressible-flow equations is well behaved for pressure-primitive variables. Besides, pressure primitive variables constitute a convenient choice for setting proper boundary conditions in FSI problems [27].

The paper is structured as follows: in section 2, we describe the constitutive equations for fluid, structure and mesh motion and their finite element weak formulation. In section 3, we introduce the partitioned algorithm and coupling conditions. In section 4 we provide details on our implementation for parallel computations. Finally, in section 5, we present the results of numerical test cases to verify and validate the numerical method on three FSI benchmarks for compressible and incompressible flows.

2. Computational method

In this section, we present the governing equations and the solution scheme for fluid, structure and mesh motion problem in the framework of FSI. Fluid flow equations are solved by space-time FEM on a deforming grid, and the solid and mesh motion equations are solved in a Lagrangian framework. The solvers are solved numerically and coupled through implicit Dirichlet-Neumann boundary conditions at each time step. We present the details in the following subsections.

2.1. Fluid equations and numerical solver

Let $\Omega_t^f \in \mathbf{R}^n$ be the time-dependent n-dimensional spatial domain for fluid with boundary Γ_t^f at time t ∈ (0,T). The governing equations is the set of Navier-Stokes equations for compressible flows:

$$\frac{\partial \rho}{\partial t} + \boldsymbol{\nabla} \cdot (\rho \boldsymbol{v}) = 0 \tag{1}$$

$$\frac{\partial \rho \boldsymbol{v}}{\partial t} + \boldsymbol{\nabla} \cdot (\rho \boldsymbol{v} \otimes \boldsymbol{v}) + \nabla p = \boldsymbol{\nabla} \cdot \boldsymbol{\tau} + \rho \boldsymbol{g} \tag{2}$$

$$\frac{\partial \rho E}{\partial t} + \boldsymbol{\nabla} \cdot (\rho E \boldsymbol{v}) + \nabla \cdot (p \boldsymbol{v}) = \boldsymbol{\nabla} \cdot (\boldsymbol{\tau} \boldsymbol{v} - \boldsymbol{q}) + \rho (\boldsymbol{g} \cdot \boldsymbol{v}) \tag{3}$$

where ρ is the density, $\boldsymbol{v}$ is the velocity, p is the pressure, $\boldsymbol{g}$ is the gravity. $\boldsymbol{\tau}$ is the viscous stress tensor and $\boldsymbol{q}$ is the heat flux vector.

$$\boldsymbol{\tau} = \lambda \boldsymbol{\nabla} \cdot \boldsymbol{v} + \mu((\boldsymbol{\nabla} \boldsymbol{v}) + (\boldsymbol{\nabla} \boldsymbol{v})^T) \tag{4}$$

$$\boldsymbol{q} = -\kappa \boldsymbol{\nabla} T \tag{5}$$

λ and μ are the viscosity coefficients, κ is the thermal conductivity and T is the temperature. The total energy E is given by:

$$E = c_v T + \frac{|\boldsymbol{v}|^2}{2} \tag{6}$$

c_v is the specific heat at constant volume.

The Navier-Stokes equations can be written in the compact form:

$$\boldsymbol{U}_{,t} + \boldsymbol{F}_{i,i}^a = \boldsymbol{F}_{i,i}^d + \boldsymbol{S} \tag{7}$$

where $\boldsymbol{U}$ is the vector of conservation variables, $\boldsymbol{F}_i^a$ and $\boldsymbol{F}_i^d$ the ith component of the advective and diffusive fluxes, respectively, and S is the source vector.

$$\boldsymbol{U}=\begin{bmatrix}\rho\\ \rho v_j\\ \rho vE\end{bmatrix}\qquad \boldsymbol{F}_i^a=\begin{bmatrix}\rho v_i\\ \rho v_j v_i+p\delta_{ji}\\ \rho v_i E+pv_i\end{bmatrix}\qquad \boldsymbol{F}_i^d=\begin{bmatrix}0\\ \tau_{ji}\\ \tau_{ij}v_j-q_i\end{bmatrix}\qquad \boldsymbol{S}=\begin{bmatrix}0\\ \rho g_i\\ \rho g_i v_i\end{bmatrix}$$

Using $\boldsymbol{Y}=\left[p,\boldsymbol{v},T\right]^T$, the vectors of pressure primitive variables we can write Eqs. (1)-(3) in quasilinear form [54,47,26,27,19] on Ω_t^f and $\forall$ t $\in$ (0,T) as

$$\boldsymbol{A}_0\boldsymbol{Y}_{,t}+\boldsymbol{A}_i\boldsymbol{Y}_{,i}=(\boldsymbol{K}_{ij}\boldsymbol{Y}_{,j})_{,i}+\boldsymbol{S}, \tag{8}$$

where $\boldsymbol{A}_0=\boldsymbol{U}_{,\boldsymbol{Y}}$, $\boldsymbol{A}_i=\boldsymbol{F}_{i,\boldsymbol{Y}}^a$ is the i^{th} Euler Jacobian matrix, $\boldsymbol{K}=[\boldsymbol{K}_{ij}]$ is the diffusivity matrix with $\boldsymbol{K}_{ij}\boldsymbol{Y}_{,j}=\boldsymbol{F}_i^d$, ans $\boldsymbol{S}$ is the source vector. $\boldsymbol{U}$ is the vector of conservation variables, $\boldsymbol{F}_i^a$ and $\boldsymbol{F}_i^d$ are the i^{th} advective and diffusive flux vectors, respectively. We obtain incompressible flow as a limiting case from the Navier-Stokes equations for compressible flow by setting coefficients of isobaric compression, β_p and isothermal expansion, α_T equal to zero. The coefficients are defined as [27]

$$\beta_p=\frac{1}{\rho}\left(\frac{\partial\rho}{\partial p}\right)_T\qquad\qquad \alpha_T=-\frac{1}{\rho}\left(\frac{\partial\rho}{\partial T}\right)_p \tag{9}$$

The essential and natural boundary conditions for Eq. (8) are represented by $\boldsymbol{Y}=\boldsymbol{g}^f$ on $(\Gamma_t^f)_g$ and $\boldsymbol{F}_i^d\boldsymbol{n}_i=\boldsymbol{h}^f$ on $(\Gamma_t^f)_h$, where $(\Gamma_t^f)_g$ and $(\Gamma_t^f)_h$ are complementary subsets of the boundary domain Γ_t^f, $\boldsymbol{n}$ is the unit normal vector, and $\boldsymbol{g}$ and $\boldsymbol{h}$ are given functions.

The Navier-Stokes Eq. (8) is solved with time-discontinuous stabilized space-time finite element method for pressure primitive variables [27,42,19,20]. In the numerical method, space and time are simultaneously discretized, resulting in space-time slabs. The mesh for the upper surface of the slab at t_{n+1} is obtained by deforming the mesh nodes of the lower surface at t_n. Let $Q_n=\Omega_t^f\times(t_n,t_{n+1})$ be the slice of space-time domain between the time levels t_n and t_{n+1} with boundary $P_n=\Gamma_t^f\times(t_n,t_{n+1})$ and discontinuous basis functions across the slab boundaries in time-direction. The space-time finite element weighted residual formulation of Eq. (8) is written as follows: given a trial function space $\mathcal{T}_n^h$ and weighting function space $\mathcal{W}_n^h$, within each Q_n, $n=0,1,\cdots,N-1$, find $\boldsymbol{Y}^h\in\mathcal{T}_n^h$ such that $\forall\ \boldsymbol{W}^h\in\mathcal{W}_n^h$ the following relation is satisfied [54,27,66]

$$\begin{aligned}
&\int_{Q_n}\left(-\boldsymbol{W}_{,t}^h\cdot\boldsymbol{U}(\boldsymbol{Y}^h)-\boldsymbol{W}_{,i}^h\cdot\boldsymbol{F}_i^a(\boldsymbol{Y}^h)+\boldsymbol{W}_{,i}^h\cdot\boldsymbol{F}_i^d(\boldsymbol{Y}^h)-\boldsymbol{W}^h\cdot\boldsymbol{S}^h\right)dQ\\
&+\int_{\Omega(t_{n+1}^-)}\boldsymbol{W}^h(t_{n+1}^-)\cdot\boldsymbol{U}\left(\boldsymbol{Y}^h(t_{n+1}^-)\right)d\Omega-\int_{\Omega(t_n^+)}\boldsymbol{W}^h(t_n^+)\cdot\boldsymbol{U}\left(\boldsymbol{Y}^h(t_n^-)\right)d\Omega\\
&+\sum_{e=1}^{(n_{el})_n}\int_{Q_n^e}(\boldsymbol{A}_i^T\ \boldsymbol{W}_i^h)\cdot\boldsymbol{\tau}\ \boldsymbol{Res}(\boldsymbol{Y}^h)dQ+\sum_{e=1}^{(n_{el})_n}\int_{Q_n^e}\nu_{DC}\boldsymbol{W}_{,i}^h\cdot\boldsymbol{U}_{,i}^h dQ\\
&-\int_{P_n}\boldsymbol{W}^h\cdot\boldsymbol{U}(\boldsymbol{Y}^h)\hat{\boldsymbol{n}}\cdot\boldsymbol{v}^m\ dP+\int_{P_n}\boldsymbol{W}^h\cdot\left(\boldsymbol{F}_i^a(\boldsymbol{Y}^h)-\boldsymbol{F}_i^d(\boldsymbol{Y}^h)\right)\hat{\boldsymbol{n}}_i\ dP=0
\end{aligned} \tag{10}$$

In the above formulation, the first and the last two integrals are the Galerkin terms obtained from the integration by parts. The second and third integrals are the jump terms to enforce continuity of the solution between consecutive slabs. The jump terms facilitate the projection of the solution in case of remeshing. The fourth integral is the SUPG stabilization term where $\boldsymbol{\tau}$ is the stabilization matrix for pressure primitive variables [66,25,27,54,72] and $\boldsymbol{Res}$ is the numerical residual of the Navier-Stokes equations. The fifth integral is the discontinuity capturing operator [66,71,9] for shocks and sharp boundary layers. $\boldsymbol{v}^m$ is the mesh velocity and $\hat{\boldsymbol{n}}$ is the outward-directed normal vector. Eq. (10) is solved by a third-order predictor-corrector algorithm [54,19].

2.2. Structure equations and numerical solver

Let $\Omega_t^s\in\mathbf{R}^n$ be the time-dependent spatial domain for structure with boundary Γ_t^s with counterparts Ω_0^s and Γ_0^s in the undeformed configuration. The motion for an elastic structure is governed by the momentum conservation equation in the undeformed domain

$$\rho_0\frac{\partial^2\boldsymbol{d}}{\partial t^2}=\boldsymbol{\nabla}\cdot(\boldsymbol{FS})+\rho_0\boldsymbol{f} \tag{11}$$

where ρ is material density, $\boldsymbol{d}$ is displacement vector, $\boldsymbol{F}=\boldsymbol{I}+\boldsymbol{\nabla d}$ is the deformation gradient tensor, $\boldsymbol{f}$ is body force and $\boldsymbol{S}$ is the second Piola-Kirchoff stress tensor which is linked to the Cauchy stress tensor $\boldsymbol{\sigma}$ through the following kinematic transformation:

$$\boldsymbol{\sigma}=J^{-1}\boldsymbol{FSF}^T \tag{12}$$

where J = $|\boldsymbol{F}|$.

Eq. (11) is solved with appropriate essential and natural boundary conditions, represented as $\boldsymbol{d}=\boldsymbol{g}^s$ on $(\Gamma_0^s)_g$ and $(\boldsymbol{FS})\boldsymbol{N}=\boldsymbol{h}^s$ on $(\Gamma_0^s)_h$, where $(\Gamma_0^s)_g$ and $(\Gamma_0^s)_h$ are the parts of Γ_t^s corresponding to the essential and natural boundary conditions. $\boldsymbol{N}$ is the outward-directed normal vector in undeformed configuration. In the Lagrangian configuration, the density ρ in the deformed configuration can be computed from the initial density ρ_0 as $\rho=\rho_0/J$.

In the present study, we employ two constitutive material models for the finite elastic deformation of the structure. The first one is the Saint-Venant Kirchhoff material model [46]

$$\boldsymbol{S} = \Big(\lambda\delta_{IJ}\delta_{KL} + \mu(\delta_{IK}\delta_{JL} + \delta_{IL}\delta_{JK})\Big)E_{KL} \tag{13}$$

where λ and μ are Lamè constants which are characteristics of each elastic material, δ is Kronecker delta function, $\boldsymbol{E} = (\boldsymbol{C} - \boldsymbol{I})/2$ is the Green-Lagrange strain tensor, $\boldsymbol{C} = \boldsymbol{F}^T\boldsymbol{F}$ is the Cauchy-Green deformation tensor.

The second employed constitutive model is the Neo-Hookean material model which is suitable for large rotation and strong compression [56]

$$\boldsymbol{S} = \frac{\mu}{\boldsymbol{J}^{\frac{2}{3}}}\Big(\boldsymbol{I} - \frac{1}{3}tr(\boldsymbol{C})\boldsymbol{C}^{-1}\Big) + \frac{\boldsymbol{J}^2 - 1}{2}\Big(\lambda + \frac{2}{3}\mu\Big)\boldsymbol{C}^{-1} \tag{14}$$

The structure Eq. (11) is solved with the semi-discrete approach. With appropriate trial and weighting function spaces d^h and w^h, respectively, the finite element variational formulation can be written as

$$\int_{\Omega_0^s} \boldsymbol{w}^h \rho_0 \frac{\partial^2 \boldsymbol{d}^h}{\partial t^2} d\Omega + \int_{\Omega_0^s} \nabla \boldsymbol{w}^h : \boldsymbol{F}^h \boldsymbol{S}^h \, d\Omega - \int_{\Omega_0^s} \boldsymbol{w}^h \rho_0 \boldsymbol{f}^h d\Omega - \int_{\Gamma_0^s} \boldsymbol{w}^h (\boldsymbol{F}\boldsymbol{S})\boldsymbol{N} d\Gamma = 0 \tag{15}$$

The spatial discretization of the above Equation is done with Galerkin FEM. This yields the following system of ordinary differential equations:

$$\boldsymbol{M}\boldsymbol{a}_{n+1} + \boldsymbol{C}\boldsymbol{v}_{n+1} + \boldsymbol{K}\boldsymbol{d}_{n+1} = \boldsymbol{f}_{n+1} \tag{16}$$

where $\boldsymbol{M}$ is the mass matrix, $\boldsymbol{C}$ is the damping matrix and $\boldsymbol{K}$ is the stiffness matrix. $\boldsymbol{a}$ and $\boldsymbol{v}$ are acceleration and velocity, respectively. Subscript denotes the time level. We use the generalised-alpha method [14] to integrate Eq. (16) in time. At each time step the Newton–Raphson method is used to solve the non-linear system of equations.

2.3. Mesh motion solver

For mesh motion, we use the elastic deformation method which has been effectively used in [62,63,34]. In this method the computational grid is considered as an elastic body and is deformed according to moving fluid-structure interface. The governing equation is given as

$$\nabla \cdot \boldsymbol{\sigma} = 0 \tag{17}$$

where $\boldsymbol{\sigma}$ is the Cauchy stress tensor. The Eq. (17) is discretized with standard Galerkin FEM [20]. To avoid excessive distortion and to maintain a better mesh quality near the moving boundaries, the Jacobian based stiffening approach is used [64].

3. FSI coupling algorithm

FSI coupling can be done in two ways: explicit and implicit [53]. In explicit-coupling the fluid flow and structure solvers integrate explicitly in time, exchanging information only one-way within a time step. The approach is computationally cheap but becomes numerically unstable when fluid-structure density ratio is large. On the other hand, in the implicit-coupling, the information is exchanged two-way within a time step through a multiple iterations loop [37]. This approach is numerically stable and robust but more expensive than the explicit one. In this work, we use an implicit method for FSI coupling. Fluid, structure and mesh motion solvers are coupled through the Dirichlet-Neumann boundary conditions:

$$\boldsymbol{v}^f = \boldsymbol{v}^s \tag{18}$$

$$\boldsymbol{\sigma}^s\boldsymbol{n}^s = -\boldsymbol{\sigma}^f\boldsymbol{n}^f \tag{19}$$

$$\boldsymbol{d}^m = \boldsymbol{d}^s \tag{20}$$

In the above equations, superscripts f, s and m denote the fluid, structure and mesh, respectively. $\boldsymbol{v}$ is velocity and $\boldsymbol{d}$ is displacement. Eqs. (18) and (19) ensures kinematic and dynamic equilibrium between the fluid and the structure. Eq. (20) ensures geometric continuity between the fluid and structure domains.

We use the Gauss-Seidel scheme for implicit coupling. In this scheme, the fluid and the solid solvers are executed sequentially. Because of this in the literature, this is also known as serial Schwarz procedure [48]. Within a time step, multiple iterations are performed to couple the different solvers. The algorithm executing the scheme is comprised of the following steps:

- Solve the flow Eq. (10) applying structure velocity $\boldsymbol{v}^s$ at fluid-structure interface as Dirichlet boundary condition, i.e. Eq. (18).
- Compute the fluid traction force $\boldsymbol{t}^f = -\boldsymbol{\sigma}^f\boldsymbol{n}^f$ acting on the interface and solve for the structure Eq. (15) applying $\boldsymbol{t}^f$ as Neumann boundary condition, i.e. Eq. (19).
- Solve the mesh motion Eq. (17) applying structure displacement $\boldsymbol{d}^s$ as Dirichlet boundary condition at interface, i.e. Eq. (20).
- Compute mesh displacement $\boldsymbol{d}^m$ and mesh velocity $\boldsymbol{v}^m = \boldsymbol{d}^m/\Delta t$ and update the fluid mesh.

Within a time step, the iteration loop ends if either the maximum allowed corrector passes are reached or when the following convergence criterion is met at the fluid-structure interface:

$$\|\boldsymbol{d}_k^s - \boldsymbol{d}_{k-1}^s\| \leq \epsilon$$

here k is the iteration number. In this work, we use $\epsilon = 10^{-6}$ m. Aitken relaxation can be used to further accelerate the convergence of Gauss–Seidel iterations [39].

Our implementation in the numerical code uses conformal fluid and solid meshes at the interface. Using a unique set of nodes at the interface ensures that the boundary conditions Eqs. (18)-(20) are accurately assigned. For non-matching meshes, additional care is needed to ensure that the coupling is done with sufficient accuracy. For non-matching meshes at the fluid-structure interface, augmented Lagrangian approach can be used [8]. To apply the fluid traction on structure Neumann boundary, we use the following relation in Eq. (15).

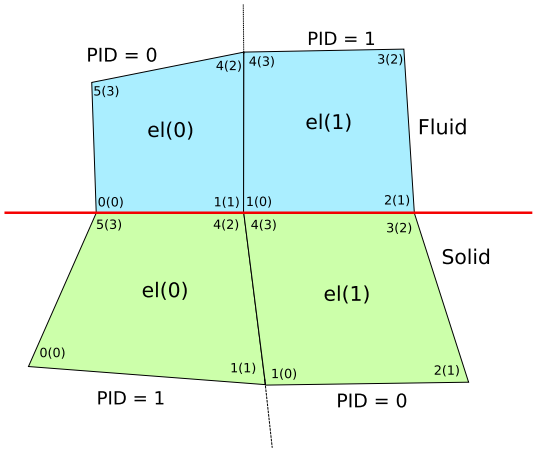

Fig. 1. An illustration of fluid-structure quadrangle elements at the interface. The domains are partitioned among two processes represented by process id (PID). Nodes are displayed as GID (LID) representing a LID-GID map (LID is local id and GID is global id). Similar LID-GID maps are constructed for elements and dofs, not shown in the figure.

$$\int_{\Gamma_0^s} \boldsymbol{w}^h(\boldsymbol{FS})\boldsymbol{N}\ d\Gamma = \int_{\Gamma_t^s} \boldsymbol{w}^h\boldsymbol{\sigma}^s\boldsymbol{n}^s\ d\Gamma = -\int_{\Gamma_t^f} \boldsymbol{w}^h\boldsymbol{\sigma}^f\boldsymbol{n}^f\ d\Gamma \tag{21}$$

To solve the large sparse system of linearized equations we use ILU preconditioned flexible block GMRES solver with a Krylov space dimension 200 and 5 restarts. The tolerance of the GMRES solver is set to 10^{-9}. The GMRES solver and ILU preconditioner are taken from the Belos package of the Trilinos library. Details on the iterative solver and the preconditioner can be found in [5].

4. Software implementation

We implemented the FSI algorithm in our in-house software GALES [42,19,20]. The software is programmed in C++ and is parallelized using OpenMPI. The software design is intended for high-performance computing and utilization of distributed memory architecture of a computer cluster. The software uses features of Boost C++ and Trilinos libraries. Here we provide the brief details on the implementation of finite element method in a parallel environment using the Trilinos library in the frame work of FSI.

As a starting point, two conformal meshes for fluid and structure are generated by the open-source software GMSH [22]. In GALES, we use the element based domain partition strategy, which means that each element is assigned to a unique process, but nodes can belong to multiple processes if they belong to the element from more than one subdomain. To partition the mesh on different processes, we use the METIS library [36], which is fast up to several million nodes. Metis allows to load balance multiple quantities simultaneously for multi-physics problems. In Metis different weights can be assigned to the elements, resulting in nearly equal total weighted partitions. Load-balancing mesh partitioning is critical for the performance of a parallel application. Each process reads and stores its submesh in a distributed manner via the process's rank in MPI_COMM_WORLD. The submeshes contain unique elements and shared nodes among process boundaries (the case of the fluid-structure boundary is shown in Fig. 1). A mapping is defined for each node, element and dof between their local (LID) and global (GID) positions on the processes. Element level matrices and vectors are constructed via the uBLAS class of boost library which provides extensive functionality for vector and matrix operations and facilitates local computations. The global sparse matrix and vector are constructed via the sparse container classes Epetra_FECrsMatrix and Epetra_FEVector, respectively, which are part of the Epetra package of the Trilinos library. The global matrix and vectors are themselves distributed with a communication pattern to exploit parallelism and are specifically designed for finite element discretizations. Finally, given the LID-GID map, the assembly of the corresponding local matrix and vector into global containers is performed with the SumIntoGlobalValues function from Epetra.

The linear solver from Belos employs the additive Schwarz method for the construction of preconditioner and solves the equations in a distributed fashion. To store the solution, the file is opened in parallel with the MPI_File_open function and the global distributed solution vector is printed in the form of chunks of data with the MPI_File_write_all function from OpenMPI. Implementation of FSI coupling in a parallel environment is a challenging task because in most cases, the interface nodes of fluid and structure meshes reside on different processes. For example node 0(0) of fluid lies on PID 0 while the corresponding matching node 5(3) of structure lies on PID 1 (Fig. 1). This poses a difficulty for node-to-node coupling. For an efficient implementation of boundary conditions the matching nodes information and the values of the coupling variable must be available at each process. To handle this we store the index numbers of fluid-solid interface nodes in a separate file while generating the meshes. We read the file in parallel and thus all processes have the information on the matching nodes. We use the MPI_Allgatherv function to collect the coupling variables.

5. Numerical results

In this section, we present three numerical examples for 2D flows, representing classical benchmarks for FSI problems. The first two cases are for incompressible flows, while the last one is for compressible flow. The incompressible problems are solved at isothermal conditions without shock-capturing term, see Eq. (10). All computations are performed over P1 and Q1 elements with 3 and 4 Gauss quadrature points, respectively. In all test cases, the mesh is refined in the vicinity of the fluid-structure interface, and fluid and structure meshes share the same interface nodal points. Apart from the fixed domain boundaries, the mesh is allowed to move everywhere. The time integration parameter ρ_∞ for the structure solver is set to 0.5. In all test cases, the Lamè parameters for the mesh motion are set to $E = 10^3$ Pa and $\nu = 0.3$.

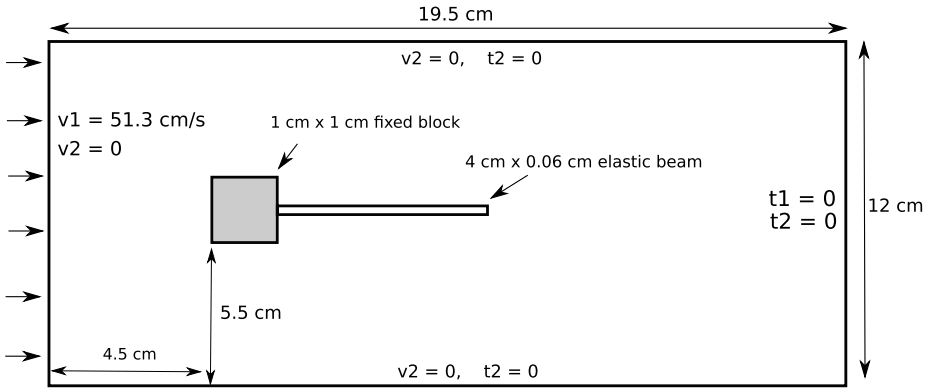

Fig. 2. Flow-induced oscillation of a flexible beam: problem setup.

Table 1
Flow-induced oscillation of a flexible beam: mesh models (m1, m2, m3 and m4): h1 is the element edge length along the rectangular outer domain; h2 is the element edge length around the rigid square; h3 is the element edge length at the fluid-solid interface.

Mesh models	m1	m2	m3	m4
h1(cm)	0.3	0.15	0.15	0.1
h2(cm)	0.09	0.045	0.045	0.03
h3(cm)	0.06	0.03	0.02	0.01
#nodes (fluid)	6215	24265	29839	77049
#elements (fluid)	12051	47777	58786	152558
#nodes (structure)	203	408	929	3562
#elements (structure)	268	542	1450	6310

Table 2
Flow-induced oscillation of a flexible beam: amplitude and frequency corresponding to the oscillations of the beam for different mesh models.

Mesh models	m1	m2	m3	m4
Amplitude (cm)	1.01	1.05	1.14	1.23
Frequency (Hz)	3.32	3.22	3.16	3.14

5.1. Flow-induced oscillation of a flexible beam

This is a classical FSI benchmark problem for incompressible flow. The problem was introduced in [68] and has been widely used for the validation of FSI numerical solvers [49,18,70,32,10,37,7].

The problem setup is displayed in Fig. 2. A flexible thin beam is attached to a fixed rigid square immersed in an incompressible flow. A uniform velocity of 51.3 cm/s is set at the inlet at a sufficiently long distance from the square. Based on the inlet velocity (v), side length of square box (L) and kinematic viscosity (ν) the value of the Reynolds number is $Re = vL/\nu = 333$. The lateral walls are slip boundaries. At the outflow, we set zero traction boundary condition. The left end of the beam is clamped to the fixed box.

The material properties are taken from [68]. The fluid density and viscosity are 1.18×10^{-3} g/cm^3 and 1.82×10^{-4} g/(cm s). The structure density is 0.1 g/cm^3, and the Young's modulus E and Poisson's ratio ν are 2.5×10^6 g/(cm s^2) and 0.35, respectively. The elastic beam is modelled with the Neo-Hookean material model (Eq. (14)) with the plane stress condition.

A mesh convergence study has been performed on this simulation case (Table 1 and Fig. 3). We start the simulation with fluid and structure set at rest and apply inlet velocity instantaneously. We use a fixed time step of 0.001 s with maximum 10 allowed corrector passes.

This test case shows general characteristics similar to those of the flow past a fixed cylinder at high Reynolds number. For all employed mesh models the flow exhibits a transient behaviour with vortices emerging and separating from the right end corners of the rigid square. These vortices induce a periodic variation of the pressure behind the square: alternatively creating a high and low pressure zones above and below the beam. This induces oscillations of the elastic beam.

Fig. 4 shows the results for pressure and velocity at several time instants for mesh model m1. In Fig. 5 we display the deformed computational mesh around the beam. Time t = 6.6 s and t = 7 s correspond, respectively, to the instants when the beam attains the maximum upward and the minimum downward displacements. As can be noticed from the figure, the mesh elements retains their good quality.

Inside the non linear loop of fluid and solid solvers the convergence is achieved within 3 corrector passes (see Fig. 6) for all employed mesh models. Fig. 7 plots the temporal profile of the vertical displacement of the tip. In all mesh models after around 2.3 seconds the oscillations of the elastic beam show a nearly periodic state. Table 2 reports the amplitude and frequency of the oscillating beam for the different employed mesh models. The observed tip vertical amplitude and oscillation frequency lie between 1.01-1.23 cm and 3.32-3.14 Hz, respectively. In particular, we notice that mesh refinement brings the computed oscillation frequency progressively closer to the theoretical Eigen-frequency value of the elastic beam (3.03). Table 3 shows that our results compare well with previous works with partitioned approach.

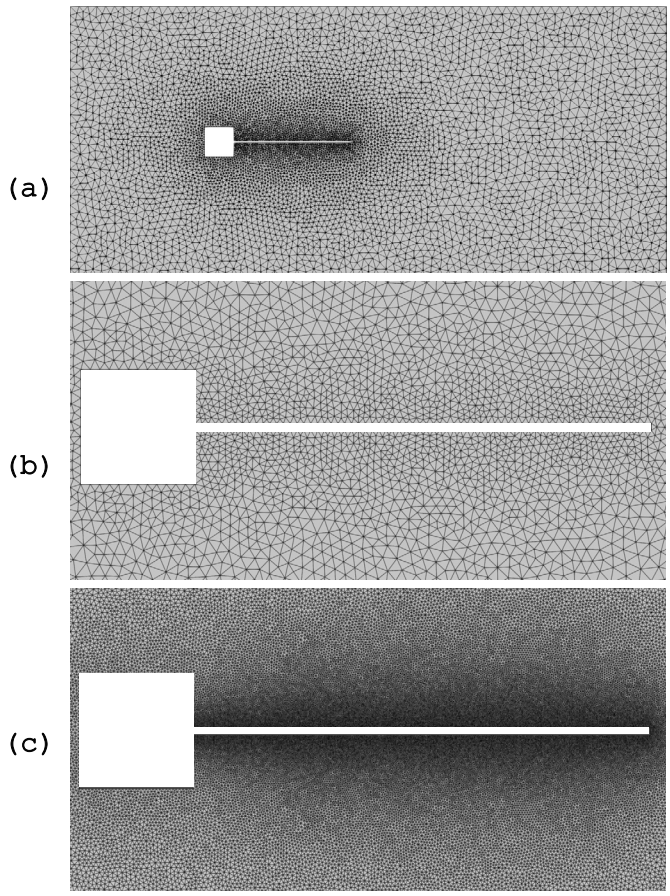

Fig. 3. Flow-induced oscillation of a flexible beam: fluid meshes: (a) mesh model m1, (b) zoomed view at the interface of mesh model m1, (b) zoomed view at the interface of mesh model m4.

Table 3
Flow-induced oscillation of a flexible beam: comparison for the vertical displacement and frequency of oscillations of the beam.

References	d (cm)	f (Hz)
Wood et al. [70]	1.15	2.94
Dettmer et al. [18]	1.1-1.4	2.96-3.31
Habchi et al. [24]	1.02	3.25
Matthies et al. [48]	1.18	3.13
Present work (m1-m4)	1.01-1.23	3.32-3.14

5.2. Vertical beam in uniform channel flow

This problem involves a vertical beam, clamped at the base, set as an obstacle in a channel flow. In [3] the authors studied the flow over backward facing step obstructed by a flexible cantilever beam into the channel. A variant of this problem was studied by placing an immersed leaflet in pulsatile flow, using the oomph-lib, an object-oriented multi-physics open-source finite-element library [28]. In [16] the authors modelled a similar problem for a restrictor in a converging channel. In [11], the authors modelled a steady flow past a vertical beam, and in [24], the problem was extended by considering two elastic flaps. The setup that we consider here corresponds to the one in [51].

The problem setup is described in Fig. 8. At the inlet a uniform velocity of 1 m/s is applied. Free outflow conditions are set at the outlet. The lateral walls are considered as slip boundaries ($v_2 = 0$; $\tau_{12} = 0$). Initial value of pressure and velocity are set to zero. The fluid and structure meshes contained 13848 and 358 elements, respectively. The fluid properties are: density = 1 kg/m^3, viscosity = 0.001 Pa s, resulting in $Re = 1000$. The structure is modelled as Saint-Venant Kirchhoff material (Eq. (13)) with plane stress condition, and density = 1000 kg/m^3, Young's modulus $E = 6 \times 10^4$ Pa, Poisson ratio $\nu = 0.35$. The simulation was run for 60 s with time step of 0.01 s and maximum 4 corrector passes.

After the immediate start of the simulation, at 0.2 s a vortex is generated due to the velocity gradient between the accelerating fluid in front and the still fluid behind the beam. The vortex is clockwise and moves downstream. Fig. 9 shows snapshots of the flow field described by instantaneous streamlines, superimposed to the pressure field. Fig. 10 shows the zoomed view of the computational mesh around the beam at times t = 0 and t = 5 s when the maximum displacement is achieved. As it can be seen from the figure the mesh remains of good quality, meaning that its elements are not excessively twisted or deformed, even after such large deformation. The tip displacement of the elastic beam is reported in Fig. 11, together with the same quantity as from the numerical simulations in [51]. The beam gets its maximum deflection at t = 5 s, after which it tends to return to its initial position and continue fluctuating for the subsequent times.

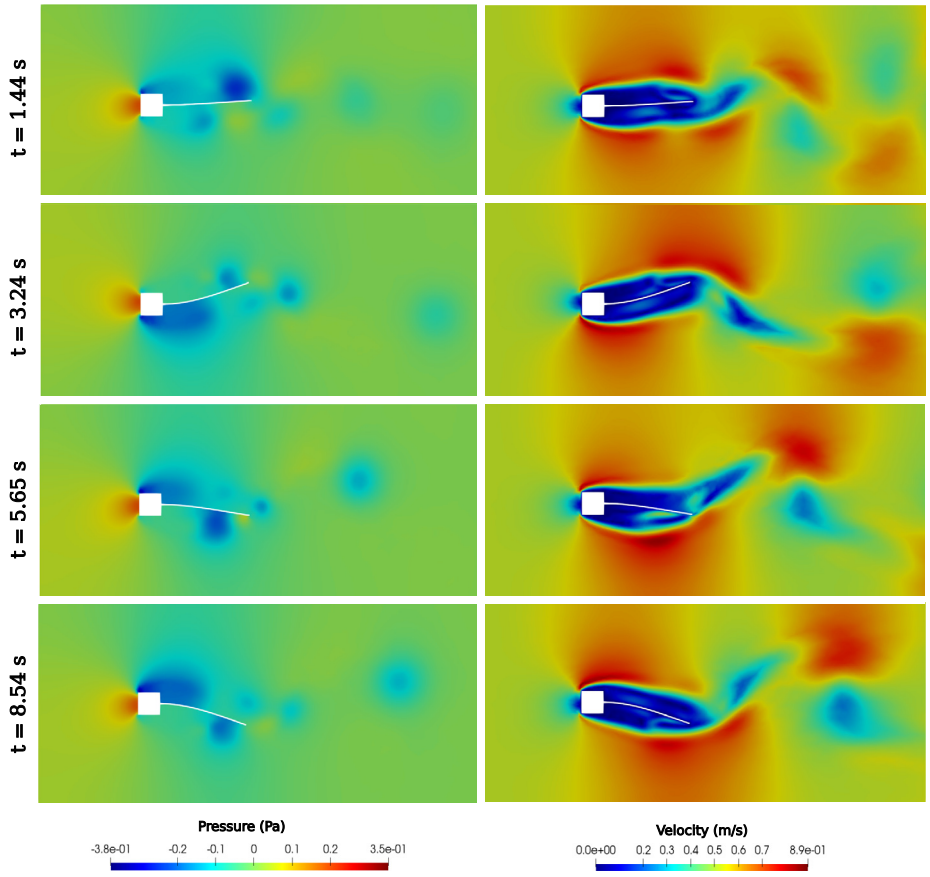

Fig. 4. Flow-induced oscillation of a flexible beam: pressure and velocity results for mesh model m1.

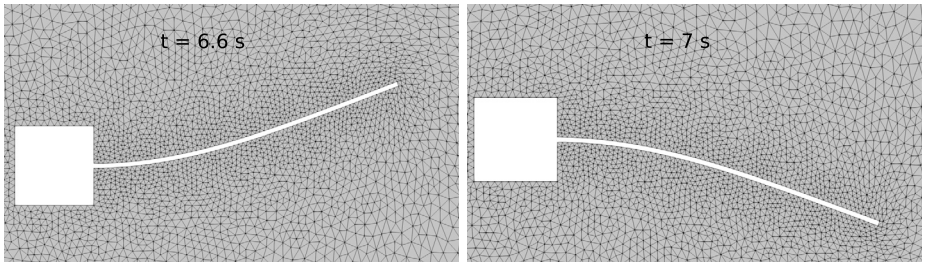

Fig. 5. Flow-induced oscillation of a flexible beam: mesh deformation for mesh model m1.

5.3. Shock-induced deflection of an elastic panel

Here we test our numerical solver for compressible flows. The test consists in computing the deflection of an elastic panel caused by a shock wave. The problem was first proposed in Giordano et al. [23] as a way to benchmark compressible transient flow solvers. The authors performed an experiment and compared the results obtained with their numerical method. Since then, the problem has been effectively used to validate compressible fluid-structure interaction solvers [17,69,2].

The problem setup is described in Fig. 12. A 1 mm wide panel is clamped into a step which is 20 mm far from the shock wave. The Mach number corresponding to the shock wave is 1.21. We use air as fluid and the ideal gas law as the equation of state. The initial pressure, temperature and velocity for the left and right sides of the shock are shown in Fig. 12. At inlet the flow variables are set equal to the left side of the shock and slip conditions are imposed on the lateral walls. At outlet no boundary condition is set. We use the finite-deformation Saint-Venant Kirchhoff material model (Eq. (13)) for the elastic panel. The material properties of the panel are as follows: density = 7600 kg/m^3, Young's modulus = 220 GPa, and Poisson ratio = 0.3. We carry out the computations to a time of 2.5 ms with a constant time step of 1 μs and maximum 5 corrector passes. The fluid and structure meshes are composed of 167065 and 1252 Q1 elements, respectively.

Fig. 13 displays the results for the pressure field at four different time instances starting from when the shock wave reaches the elastic panel. For comparison with [23], we take the instance when the wave strikes with the panel as t = 0 μs. A part of the shock wave reflects after striking with the step. However, the larger part of the wave reaches the elastic panel and gives rise to patterns associated with wave transmission in the downstream direction and reflection in the upstream direction, well visible at subsequent times. Our simulation results were able to capture the mutual interaction of the reflecting waves coming from the step, elastic panel and the lateral boundaries. Simulation results also display the

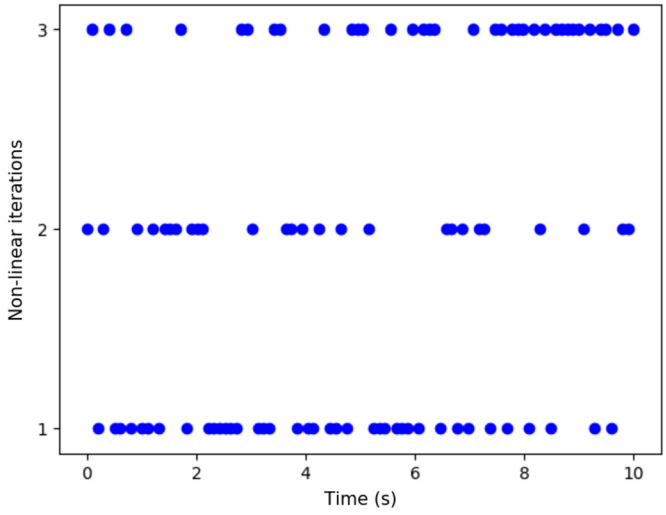

Fig. 6. Flow-induced oscillation of a flexible beam: non-linear iterations per time step to achieve convergence for mesh model m1.

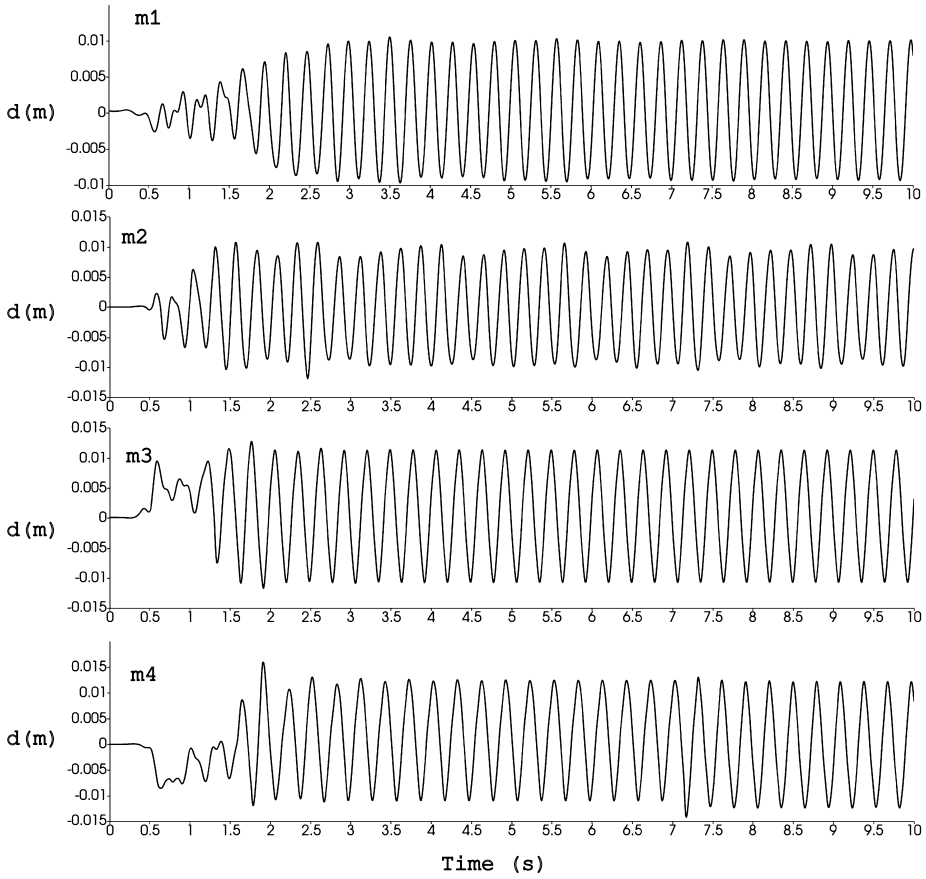

Fig. 7. Flow-induced oscillation of a flexible beam: vertical displacement of the tip of the beam for the four employed mesh models m1 to m4.

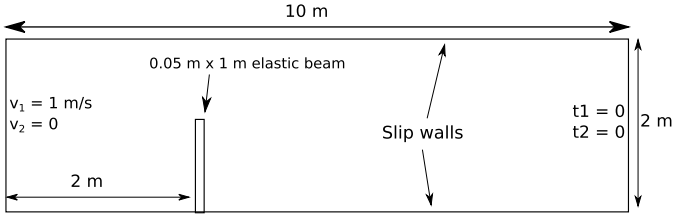

Fig. 8. Vertical beam in uniform channel flow: problem setup.

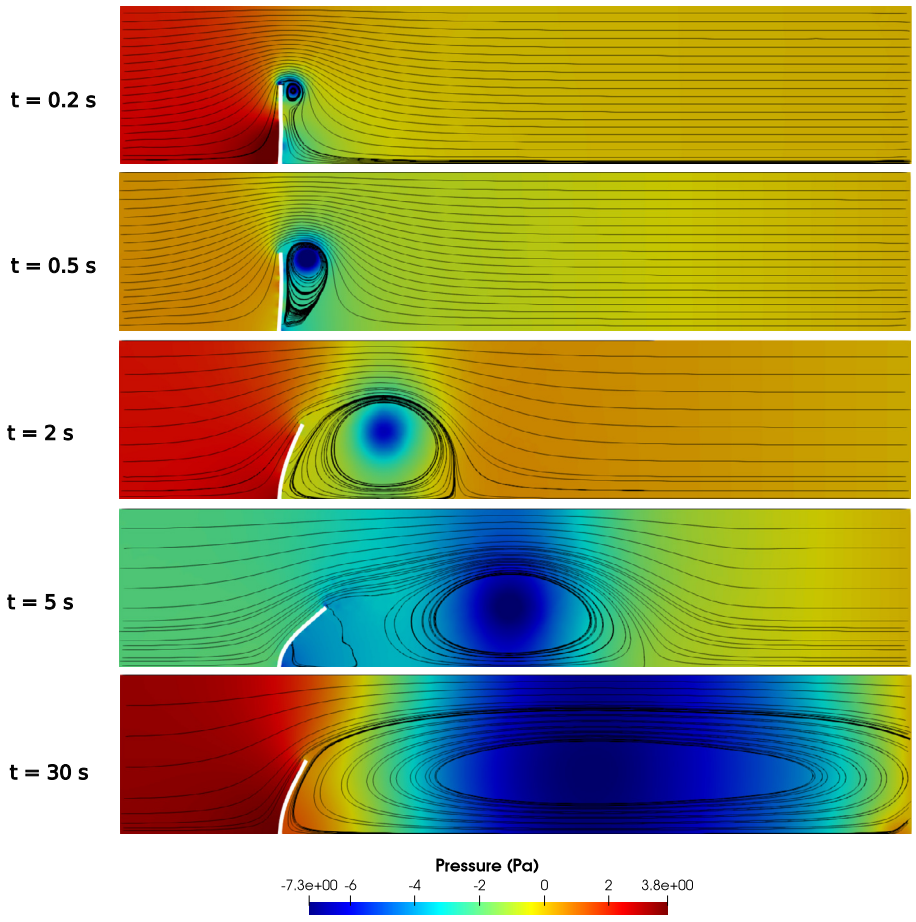

Fig. 9. Vertical beam in uniform channel flow: snapshots of flow field with streamlines and pressure distribution.

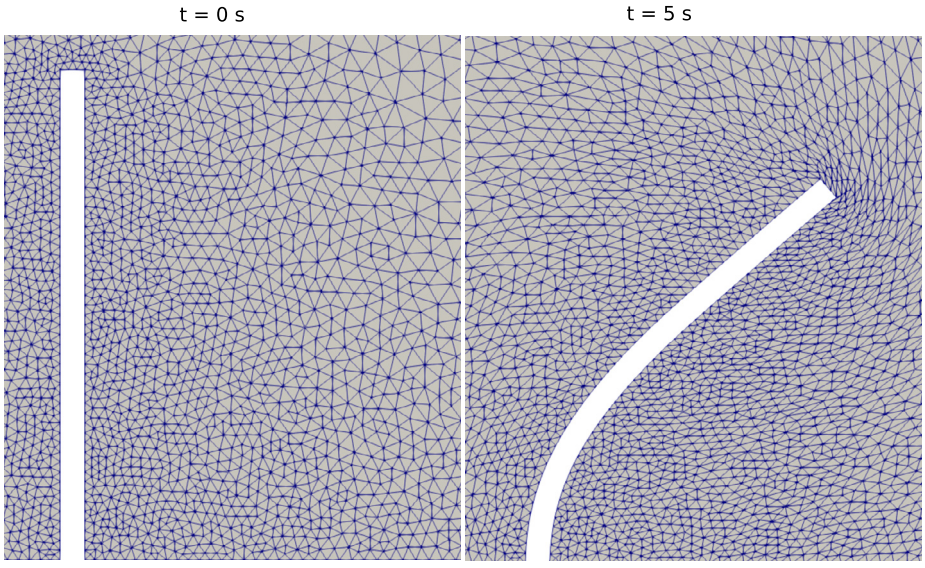

Fig. 10. Vertical beam in uniform channel flow: clipped zoom of initial and deformed mesh around the elastic beam.

generation of a low pressure area at the panel trailing end and the roll-up of shear layers which eventually form a vortex. At subsequent times the separation of the vortex from the panel as well as the further movement of the shock wave in downstream direction can be noticed.

In Fig. 14 we compares the present simulation results for the numerical schlieren (the magnitude of the density gradient vector) with the experimental and numerical results obtained in [23]. The motion of the vortex and the shape of the reflected and transmitted waves agree well with the results reported in [23].

Fig. 15 shows the computed horizontal displacement of the tip of the panel. The forward and backward deflection of the panel is due to impinging of the shock wave and stored elastic energy, respectively. Our results are in excellent agreement with the experiments, both in terms of deformation

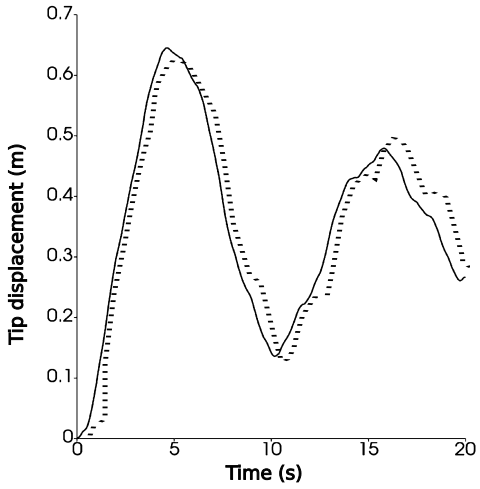

Fig. 11. Vertical beam in uniform channel flow: comparison for the tip displacement of the beam: [51] (dashed line) and present work (solid line).

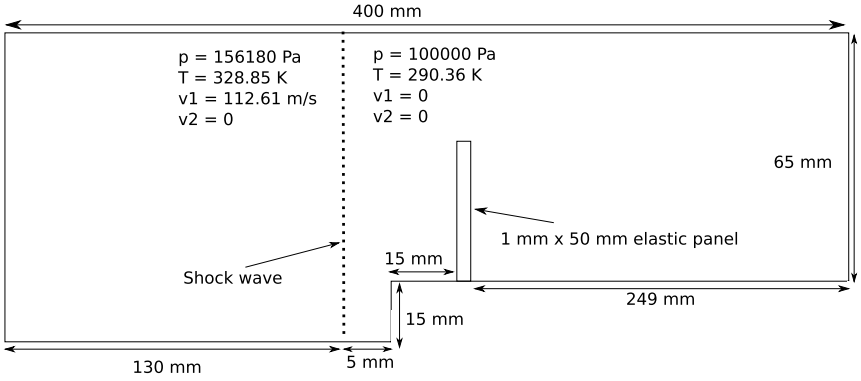

Fig. 12. Shock-induced deflection of an elastic panel: problem setup.

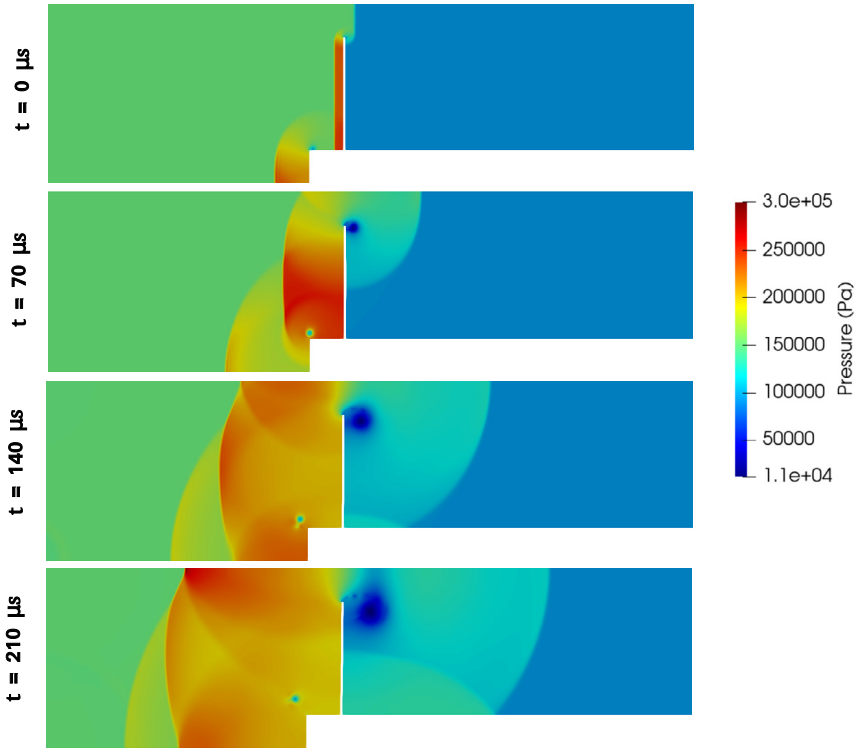

Fig. 13. Shock-induced deflection of an elastic panel: pressure field. In the figure time 0 μs corresponds to the instance when the shock wave impacts the panel.

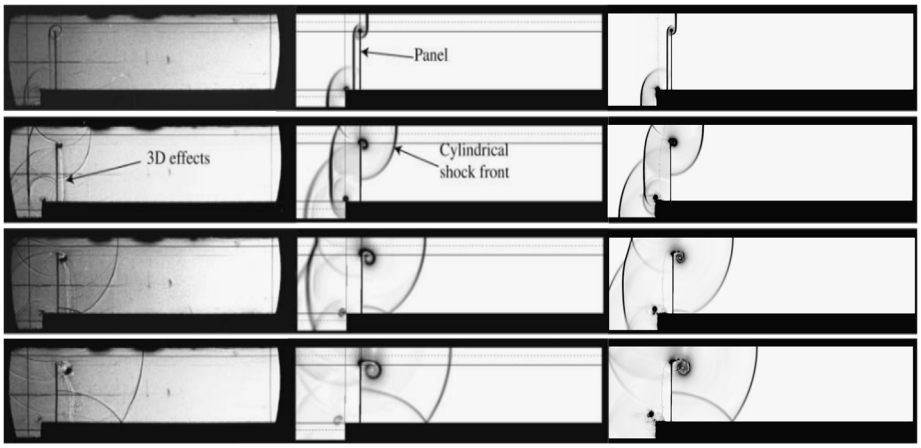

Fig. 14. Shock-induced deflection of an elastic panel: the left and the middle columns show the experimental shadowgraph and numerical schlieren, respectively, from [23], and the right column is numerical schlieren from the present results. The time instants are 0, 70, 140 and 210 μs. Time 0 μs corresponds to the instance when the shock wave impacts the panel.

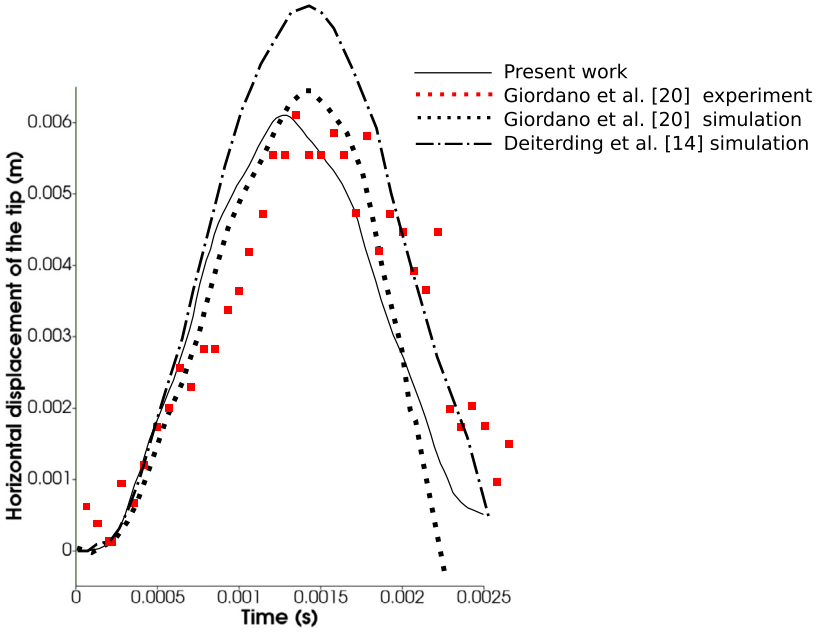

Fig. 15. Shock-induced deflection of an elastic panel: Horizontal deflection of the tip. The present results are compared with experimental and numerical data.

pattern and maximum deformation attained. By comparison, the simulation results in [23] show a too rapid return to the initial position, and those in [17] significantly overestimate the maximum deformation.

6. Concluding remarks

In this article, which extends our previous work on compressible and incompressible flow in fixed domains [19] and free surface flow in moving domains [20], we present a partitioned algorithm for strongly coupled FSI problems. In particular, we illustrate the flow solver formulation with the stabilized finite element method based on Galerkin least squares and discontinuity capturing terms, and the solver for structure elasto-mechanics and mesh motion based on standard Galerkin FEM. We solved the structure mechanics and mesh motion equations with standard Galerkin FEM. We successfully validate our numerical code on widely used benchmarks and demonstrate the capability of the method to tackle both compressible and incompressible flow problems, classically approached with a variety of different numerical algorithms, using only one single set of variables. The efficiency and robustness of the method makes it ideal to investigate practical problems in a variety of situations which are relevant in natural systems as well as industrial applications, in particular where compressible and incompressible flows coexist and fluid-structure interactions cannot be neglected.

Link to the Reproducible Capsule

https://codeocean.com/capsule/6716089/tree/v1

Acknowledgements

The authors gratefully acknowledge the anonymous reviewers for their helpful comments on the originally submitted manuscript.

References

[1] A. Aravena, et al., Conduit stability effects on intensity and steadiness of explosive eruptions, Sci. Rep. 8 (4125) (2018) 1–9.
[2] S. Bailoor, et al., Fluid-structure interaction solver for compressible flows with applications to blast loading on thin elastic structures, Appl. Math. Model. 52 (2017) 470–492.
[3] K.J. Bathe, H. Zhang, Finite element developments for general fluid flows with structural interactions, Int. J. Numer. Methods Eng. 60 (2004) 213–232.
[4] J. Batina, Unsteady Euler algorithm with unstructured dynamic mesh for complex-aircraft aerodynamic analysis, AIAA J. 29 (3) (1991) 327–333.
[5] E. Bavier, et al., Amesos2 and Belos: direct and iterative solvers for large sparse linear systems, Sci. Program. 20 (3) (2012) 241–255.
[6] Y. Bazilevs, et al., Isogeometric fluid-structure interaction analysis with applications to arterial blood flow, Comput. Mech. 38 (2006) 310–322.
[7] Y. Bazilevs, et al., Isogeometric fluid-structure interaction: theory, algorithms, and computations, Comput. Mech. 43 (2008) 3–37.
[8] Y. Bazilevs, et al., Isogeometric fluid-structure interaction analysis with emphasis on non-matching discretizations, and with application to wind turbines, Comput. Methods Appl. Mech. Eng. 249–252 (2012) 28–41.
[9] Y. Bazilevs, et al., Gas turbine computational flow and structure analysis with isogeometric discretization and a complex-geometry mesh generation method, Comput. Mech. 67 (2021) 57–84.
[10] Friedrich-Karl Benra, et al., A comparison of one-way and two-way coupling methods for numerical analysis of fluid-structure interactions, J. Appl. Math. 2011 (853560) (2011) 1–16.
[11] A.E.J. Bogaer, et al., An evaluation of quasi-Newton methods for application to FSI problems involving free surface flow and solid body contact, Comput. Struct. 173 (2016) 71–83.
[12] F. Charbel, et al., Provably second-order time-accurate loosely-coupled solution algorithms for transient nonlinear computational aeroelasticity, Comput. Methods Appl. Mech. Eng. 195 (17–18) (2006) 1973–2001.
[13] Z.J. Chen, A.J. Przekwas, A coupled pressure-based computational method for incompressible/compressible flows, J. Comput. Phys. 229 (2010) 9150–9165.
[14] J. Chung, J.M. Hulbert, A time integration algorithm for structural dynamics with improved numerical dissipation: the generalized-alpha method, J. Appl. Mech. 60 (2) (1993) 371–375.
[15] G.A. Davis, O.O. Bendiksen, Unsteady transonic two-dimensional Euler solutions using finite elements, AIAA J. 31 (6) (1993) 1051–1059.
[16] J. Degroote, et al., Performance of a new partitioned procedure versus a monolithic procedure in fluid-structure interaction, Comput. Struct. 87 (11–12) (2009) 793–801.
[17] R. Deiterding, et al., Parallel adaptive fluid-structure interaction simulation of explosions impacting on building structures, Comput. Fluids 88 (2013) 719–729.
[18] W. Dettmer, D. Peric, A computational framework for fluid-structure interaction: finite element formulation and applications, Comput. Methods Appl. Mech. Eng. 195 (41–43) (2006) 5754–5779.
[19] D. Garg, et al., Computation of compressible and incompressible flows with a space-time stabilized finite element method, Comput. Math. Appl. 75 (12) (2018) 4272–4285.
[20] D. Garg, et al., Modeling free surface flows using stabilized finite element method, Math. Probl. Eng. 2018 (6154251) (2018) 1–9.
[21] D. Garg, et al., Long-lived compositional heterogeneities in magma chambers, and implications for volcanic hazard, Sci. Rep. 9 (3321) (2019) 1–13.
[22] C. Geuzaine, J.F. Remacle, Gmsh: a three-dimensional finite element mesh generator with built-in pre- and post-processing facilities, Int. J. Numer. Methods Eng. 79 (11) (2009) 1309–1331.
[23] J. Giordano, et al., Shock wave impacts on deforming panel, an application of fluid-structure interaction, Shock Waves 14 (2005) 103–110.
[24] C. Habchi, et al., Partitioned solver for strongly coupled fluid–structure interaction, Comput. Fluids 71 (2013) 306–319.
[25] G. Hauke, Simple stabilizing matrices for the computation of compressible flows in primitive variables, Comput. Methods Appl. Mech. Eng. 190 (51–52) (2001) 6881–6893.
[26] G. Hauke, T.J.R. Hughes, A unified approach to compressible and incompressible flows, Comput. Methods Appl. Mech. Eng. 113 (3) (1994) 389–395.
[27] G. Hauke, T.J.R. Hughes, A comparative study of different sets of variables for solving compressible and incompressible flows, Comput. Methods Appl. Mech. Eng. 153 (1–2) (1998) 1–44.
[28] M. Heil, et al., Solvers for large-displacement fluid-structure interaction problems: segregated versus monolithic approaches, Comput. Mech. 43 (2008) 91–101.
[29] T.B. Helenbrook, Mesh deformation using the biharmonic operator, Int. J. Numer. Methods Eng. 56 (7) (2001) 1–30.
[30] M. Hsu, Y. Bazilevs, Fluid-structure interaction modeling of wind turbines: simulating the full machine, Comput. Mech. 50 (2012) 821–833.
[31] M.C. Hsu, Y. Bazilevs, Blood vessel tissue prestress modeling for vascular fluid-structure interaction simulations, Finite Elem. Anal. Des. 47 (2011) 593–599.
[32] B. Hubner, et al., A monolithic approach to fluid-structure interaction using space-time finite elements, Comput. Methods Appl. Mech. Eng. 193 (23–26) (2004) 2087–2104.
[33] T.J.R. Hughes, The Finite Element Method: Linear Static and Dynamic Finite Element Analysis, Prentice Hall Inc., Engelwood Cliffs, New Jersey, 1987, 07632.
[34] A.A. Johnson, T.E. Tezduyar, Mesh update strategies in parallel finite element computations of flow problems with moving boundaries and interfaces, Comput. Methods Appl. Mech. Eng. 119 (1–2) (1994) 73–94.
[35] R. Kamakoti, W. Shyy, Fluid-structure interaction for aeroelastic applications, Prog. Aerosp. Sci. 40 (8) (2004) 535–558.
[36] G. Karypis, V. Kumar, A fast and high quality multilevel scheme for partitioning irregular graphs, SIAM J. Sci. Comput. 20 (1) (1999) 359–392.
[37] C. Kassiotis, et al., Nonlinear fluid-structure interaction problem. Part I: Implicit partitioned algorithm, nonlinear stability proof and validation example, Comput. Mech. 47 (2011) 305–323.
[38] S. Kornet, et al., Thermal-fsi modeling of flow and heat transfer in a heat exchanger based on minichanels, J. Power Technol. 97 (5) (2017) 373–381.
[39] U. Kuttler, W. Wall, Fixed-point fluid-structure interaction solvers with dynamic relaxation, Comput. Mech. 43 (2008) 61–72.
[40] B. Lofti, et al., 3D fluid-structure interaction (FSI) simulation of new type vortex generators in smooth wavy fin-and-elliptical tube heat exchanger, Eng. Comput. 33 (8) (2016) 2504–2529.
[41] R. Löhner, C. Yang, Improved ale mesh velocities for moving boundaries, Commun. Numer. Methods Eng. 12 (10) (1996) 599–608.
[42] A. Longo, et al., A finite element Galerkin/least squares method for computation of multicomponent compressible incompressible flows, Comput. Fluids 67 (2012) 57–71.
[43] A. Longo, et al., Magma convection and mixing dynamics as a source of ultra-long-period oscillations, Bull. Volcanol. 74 (2012) 873–880.
[44] D.R. Lynch, Unified approach to simulation on deforming elements with application to phase change problems, J. Comput. Phys. 47 (3) (1982) 387–411.
[45] A. Malossi, et al., Algorithms for the partitioned solution of weakly coupled fluid models for cardiovascular flows, Int. J. Numer. Methods Biomed. Eng. 27 (2011) 2035–2057.
[46] J.E. Marsden, T.J.R. Hughes, Mathematical Foundations of Elasticity, Dover Publications Inc., New York, 1993.
[47] A. Masud, T.J.R. Hughes, A space-time Galerkin/least-squares finite element formulation of the Navier-Stokes equations for moving domain problems, Comput. Methods Appl. Mech. Eng. 146 (1–2) (1997) 91–126.
[48] H. Matthies, et al., Algorithms for strong coupling procedures, Comput. Methods Appl. Mech. Eng. 195 (17–18) (2006) 2028–2049.
[49] H.G. Matthies, J. Steindorf, Partitioned strong coupling algorithms for fluid-structure interaction, Comput. Struct. 81 (8–11) (2003) 805–812.
[50] A. Munjiza, et al., FSIS: a novel fluid–solid interaction solver for fracturing and fragmenting solids, Comput. Part. Mech. 7 (2020) 789–805.
[51] M. Olivier, et al., A fluid-structure interaction solver for nano-air-vehicle flapping wings, in: 19th AIAA Computational Fluid Dynamics Conference, San Antonio, 2009, pp. 1–15, 2009-3676.
[52] P. Papale, et al., Pressure evolution in shallow magma chambers upon buoyancy-driven replenishment, Geochem. Geophys. Geosyst. 18 (3) (2017) 1214–1224.
[53] M. Schafer, et al., An Implicit Partitioned Method for the Numerical Simulation of Fluid–Structure Interaction, Lecture Notes in Computational Science and Engineering, Springer, Berlin, Heidelberg, 2006.
[54] F. Shakib, et al., A new finite element formulation for computational fluid dynamics: X. The compressible Euler and Navier-Stokes equations, Comput. Methods Appl. Mech. Eng. 89 (1–3) (1991) 141–219.
[55] W. Shyy, et al., Flexible Wings and Fluid-Structure Interactions for Micro-Air Vehicles. Flying Insects and Robots, Springer, Berlin, Heidelberg, 2009.
[56] J.C. Simo, T.J.R. Hughes, Computational Inelasticity, Springer, New York, 1998.
[57] M. Souli, et al., ALE formulation for fluid-structure interaction problems, Comput. Methods Appl. Mech. Eng. 190 (1–2) (2000) 659–675.
[58] K. Takizawa, et al., Space-time fsi modeling and dynamical analysis of spacecraft parachutes and parachute clusters, Comput. Mech. 48 (2011) 345–364.

[59] K. Takizawa, T.E. Tezduyar, Computational methods for parachute fluid-structure interactions, Arch. Comput. Methods Eng. 19 (2012) 125–169.
[60] T. Terahara, et al., Heart valve isogeometric sequentially-coupled fsi analysis with the space–time topology change method, Comput. Mech. 65 (2020) 1167–1187.
[61] C. Textor, et al., Numerical simulation of explosive volcanic eruptions from the conduit flow to global atmospheric scales, Ann. Geophys. 48 (4/5) (2005) 817–842.
[62] T.E. Tezduyar, M. Behr, A new strategy for finite element computations involving moving boundaries and interfaces- the deforming-spatial-domain/space-time procedure: I. The concept and the preliminary numerical tests, Comput. Methods Appl. Mech. Eng. 94 (3) (1992) 339–351.
[63] T.E. Tezduyar, M. Behr, A new strategy for finite element computations involving moving boundaries and interfaces-the deforming-spatial-domain/space-time procedure: II. computation of free-surface flows, two-liquid flows, and flows with drifting cylinders, Comput. Methods Appl. Mech. Eng. 94 (3) (1992) 353–371.
[64] T.E. Tezduyar, et al., Computation of Unsteady Incompressible Flows with the Stabilized Finite Element Methods-Space-Time Formulations, Iterative Strategies and Massively Parallel Implementations, New Methods in Transient Analysis, vol. 143, 1992, pp. 7–24.
[65] T.E. Tezduyar, et al., Fluid-structure interaction modeling of ringsail parachutes, Comput. Mech. 43 (2008) 133–142.
[66] T.E. Tezduyar, M. Senga, Stabilization and shock-capturing parameters in SUPG formulation of compressible flows, Comput. Methods Appl. Mech. Eng. 195 (2006) 1621–1632.
[67] E. Walhorn, et al., Fluid-structure coupling within a monolithic model involving free surface flows, Comput. Struct. 83 (25–26) (2005) 2100–2111.
[68] W. Wall, Fluid–Structure Interaction with Stabilized Finite Elements, PhD thesis, University of Stuttgart, 1999.
[69] Wang Li, et al., An immersed boundary method for fluid-structure interaction with compressible multiphase flows, J. Comput. Phys. 346 (2017) 131–151.
[70] C. Wood, et al., Partitioned block-Gauss-Seidel coupling for dynamic fluid-structure interaction, Comput. Struct. 88 (23–24) (2010) 1367–1382.
[71] Fei Xu, et al., Compressible flows on moving domains: stabilized methods, weakly enforced essential boundary conditions, sliding interfaces, and application to gas-turbine modeling, Comput. Fluids 158 (2017) 201–220.
[72] Fei Xu, et al., Immersogeometric analysis of compressible flows with application to aerodynamic simulation of rotorcraft, Math. Models Methods Appl. Sci. 29 (5) (2019) 905–938.
[73] Y. Bazilevs, et al., Variational multiscale residual-based turbulence modeling for large eddy simulation of incompressible flows, Comput. Methods Appl. Mech. Eng. 197 (1) (2007) 173–201.
[74] T. Yamamoto, K. Takatani, Pressure-based unified solver for gas-liquid two-phase flows where compressible and incompressible flows coexist, Int. J. Numer. Methods Fluids 88 (6) (2018) 277–295.
[75] L. Zhang, et al., Fem simulation of turbulent flow in a turbine blade passage with dynamical fluid-structure interaction, Int. J. Numer. Methods Fluids 61 (12) (2009) 1299–1330.
[76] O.C. Zienkiewicz, et al., Compressible and incompressible flow; an algorithm for all seasons, Comput. Methods Appl. Mech. Eng. 78 (1990) 105–121.